PHYSICAL REVIEW B **98**, 045407 (2018)

Crystal-field effects in graphene with interface-induced spin-orbit coupling

Tarik P. Cysne,[1,*] Aires Ferreira,[2,†] and Tatiana G. Rappoport[1]
[1]Instituto de Física, Universidade Federal do Rio de Janeiro, Caixa Postal 68528, Rio de Janeiro 21941-972, Rio de Janeiro, Brazil
[2]Department of Physics, University of York, York YO10 5DD, United Kingdom

(Received 13 April 2018; published 9 July 2018)

We consider theoretically the influence of crystalline fields on the electronic structure of graphene placed on a layered material with reduced symmetry and large spin-orbit coupling (SOC). We use a perturbative procedure combined with the Slater-Koster method to derive the low-energy effective Hamiltonian around the K points and estimate the magnitude of the effective couplings. Two simple models for the envisaged graphene-substrate hybrid bilayer are considered, in which the relevant atomic orbitals hybridize with either top or hollow sites of the graphene honeycomb lattice. In both cases, the interlayer coupling to a crystal-field-split substrate is found to generate highly anisotropic proximity spin-orbit interactions, including in-plane "spin-valley" coupling. Interestingly, when an anisotropic intrinsic-type SOC becomes sizable, the bilayer system is effectively a quantum spin Hall insulator characterized by in-plane helical edge states robust against the Bychkov-Rashba effect. Finally, we discuss the type of substrate required to achieve anisotropic proximity-induced SOC and suggest possible candidates to further explore crystal-field effects in graphene-based heterostructures.

DOI: 10.1103/PhysRevB.98.045407

I. INTRODUCTION

The impact of the crystal environment on atomic states is pivotal to understand the electronic structure of solids containing transition-metal atoms [1]. For instance, in high-T_c cuprates, crystal-field states are essential in the description of CuO_2 planes, where Cu^{+2} ions are surrounded by elongated octahedral structures of O atoms [2,3]. The crystal-electric-field effect and its interplay with spin-orbit coupling plays an important role in magnetic anisotropy [4,5], the Jahn-Teller effect [6–8], distortive order [9], and the cooperative Jahn-Teller effect [10].

More recently, it has been appreciated that the crystal-field effect (CFE) underlies rich spin-dependent phenomena at metallic interfaces. For instance, the broken rotational symmetry of magnetic atoms in metal bilayers was found to render spin currents anisotropic [11], while a staggered CFE associated with nonsymmorphic structures of metal species is responsible for a giant enhancement of the Rashba effect in $BaNiS_2$ [12]. Here, we investigate the electronic properties of graphene placed on nonmagnetic substrates characterized by a sizable CFE. Graphene-substrate hybrid bilayers are currently attracting enormous interest due to the combination of Dirac fermions and prominent interfacial spin-orbital effects in the atomically thin (two-dimensional) limit [13–15]. Monolayers of group-VI transition-metal dichalcogenides (TMDs) are a particularly suitable match to graphene as a high-SOC substrate. The peculiar spin-valley coupling in the TMD electronic structure [16–18] provides a unique all-optical method for injection of spin currents across graphene-TMD interfaces [19,20], as recently demonstrated [21,22]. Furthermore, the proximity coupling of graphene to a TMD base breaks the sublattice symmetry of pristine graphene, leading to competing spin-valley and Bychkov-Rashba spin-orbit interactions [23–30]. The enhanced spin-orbit coupling (SOC) paves the way to *bona fide* relativistic transport phenomena in systems of two-dimensional Dirac fermions, including the inverse spin-galvanic effect [31,32].

On a qualitative level, the band structure of graphene weakly coupled to a high-SOC substrate can be understood from symmetry. The intrinsic SOC of graphene is invariant under the full symmetries of point group D_{6h}, which includes sixfold rotations and mirror inversion about the plane [33]. The reduction of the full point group in heterostructures is associated with the emergence of other interactions [34,35]. For example, interfacial breaking of inversion symmetry reduces the point group $D_{6h} \to C_{6v}$, allowing finite (nonzero) Bychkov-Rashba SOC [36]. The low-energy Hamiltonian compatible with time-reversal symmetry is

$$\mathcal{H}_{C_{6v}} = \hbar\, v(\tau_z k_x \sigma_x + k_y \sigma_y) + \lambda_{\mathrm{KM}}\, \sigma_z \tau_z s_z + \lambda_{\mathrm{R}}\, (s_x \sigma_y - \tau_z s_y \sigma_x), \tag{1}$$

where v is the Fermi velocity of massless Dirac fermions, $\mathbf{k} = (k_x, k_y)$ is the wave vector around a Dirac point (valley), and τ_i, σ_i, and s_i are Pauli matrices acting on valley, sublattice, and spin spaces, respectively. Here, λ_{KM} (λ_{R}) are the energy scales of the intrinsic-type SOC (Bychkov-Rashba) interaction enhanced by the proximity effect.

In addition, the interaction of graphene with an atomically flat substrate renders the two carbon sublattices inequivalent, further reducing the point group $C_{6v} \to C_{3v}$. A well-studied example is graphene on semiconducting TMD monolayers in the group-VI family. The hybridization between p_z electrons and the TMD orbitals generates a spin-valley term $\lambda_{\mathrm{sv}} s_z \tau_z$ in the continuum model, reflecting the generally different

---

[*] tarik@if.ufrj.br
[†] aires.ferreira@york.ac.uk

effective SOCs on A and B sublattices [24,37]. The breaking of sublattice symmetry also generates a mass term $m\sigma_z$ (of orbital origin), which can exceed tens of meV in rotationally aligned van der Waals heterostructures [38,39]. Another example of reduced symmetry occurs in graphene with intercalated Pb nanoislands [40], where a rectangular superlattice potential leads to an in-plane spin-valley coupling $\lambda^y_{\text{sv}}\tau_z s_y$ in Eq. (1). Finally, if time-reversal symmetry is broken, e.g., using a ferromagnetic substrate, a number of other spin-orbit terms are generally allowed [41].

Below, we show that the above picture is further enriched when π electrons in graphene experience a crystal-field environment via hybridization to crystal-split states. The interlayer coupling to a low-symmetry substrate removes the rotational invariance from the effective Hamiltonian (1), leading to a proliferation of spin-orbit interactions, including in-plane spin-valley ($\lambda^y_{\text{sv}}\tau_z s_y$) and anisotropic intrinsic-type ($\lambda^y_{\text{KM}}\tau_z\sigma_z s_y$) SOCs. To estimate the strength of the proximity spin-orbit interactions, we consider a minimal tight-binding model for a hybrid bilayer with hopping parameters obtained from the Slater-Koster method [42,43]. We present explicit calculations for two idealized substrates, in which a commensurate monolayer of heavy atoms sits at the hollow and top sites of pristine graphene. Finally, a Löwdin perturbation scheme is employed to obtain the low-energy continuum Hamiltonian. As a concrete example, we then discuss the possibility of obtaining an enhanced in-plane spin-valley coupling in a hybrid heterostructure of graphene and a group-IV dichalcogenide monolayer. This paper is organized as follows. In Sec. II, we introduce the substrate model and discuss how the eigenstates of free atomic shells are affected by CFE. In Sec. III, we derive the effective Hamiltonian, when the emergent rotational symmetry $C_{v\infty}$ is broken by the crystal-field environment. In Sec. IV, we address the scenario where, added to CFE, the point group C_{6v} is reduced by a sublattice-dependent interaction with atoms of the substrate, which gives rise to new types of SOCs. In Sec. V, we discuss possible realizations with group-IV TMD monolayers. Section VI presents our conclusions.

II. SUBSTRATE MODEL

We assume a sufficiently weak interlayer interaction between graphene and the substrate [37,41,44], so that the electronic states near the Fermi level derive mostly from p_z (graphene) states. Since we are mainly interested in the interplay between CFE and SOC, we shall focus on substrates containing transition-metal atoms. We focus on atomic species with an outer free shell formed by d states ($l = 2$). The electronic states of a free atom are complex wave functions with well-defined angular momentum projection. When an ion is placed in a crystalline environment, its electronic states suffer distortions due to the electric field generated by the surrounding atoms. For d ($l = 2$) atomic states, this effect is usually stronger than the spin-orbit interaction itself, which can then be treated as a perturbation [1]. The electronic states of a free atom are $(2l + 1)$-fold degenerate (neglecting relativistic corrections), but when the atom is placed in a low-symmetry environment, the degeneracy is lifted [see Fig. 1(a)]. Depending on the crystal symmetry, some of the original complex atomic states combine to form real atomic states with no defined angular momentum projection. If the symmetry is sufficiently low, as in an orthorhombic crystal, the degeneracy is fully lifted [see Fig. 1(b)], and the atomic wave functions are real.

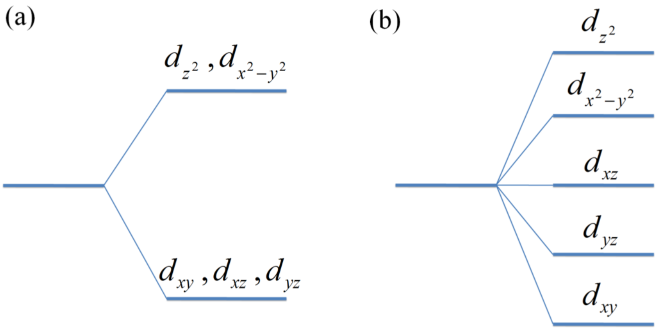

FIG. 1. Two examples of crystal-field splitting: (a) octahedral and (b) orthorhombic.

The Hamiltonian is written as $H = H_g + H_{\text{at}} + V$, where H_g is the standard nearest-neighbor tight-binding Hamiltonian for π electrons in graphene and V is the interlayer interaction. To simplify the analysis, hopping processes within H_{at}, as well as disorder effects, are neglected. Such an approximation suffices for a qualitative description of the effective (long-wavelength) interactions mediated on graphene [45]. Finally, we assume a general low-symmetry environment, such that the atomic Hamiltonian for the external free-shell subspace reads $H_{\text{at}} = H_0 + H_{\text{so}}$, with

$$H_0 = \sum_i \sum_{s=\uparrow,\downarrow} \sum_{d_l} \epsilon_{d_l} |d_l,s,i\rangle\langle i,s,d_l|, \tag{2}$$

$$H_{\text{so}} = \sum_i \xi\, \vec{l}_i \cdot \vec{s}_i., \tag{3}$$

where i runs over the substrate atoms and $\vec{l}_i$ ($\vec{s}_i$) is the associated dimensionless orbital (spin) angular momentum operator. The first term [Eq. (2)] describes the crystal-field splitting of d levels [46]. The second term [Eq. (3)] is the spin-orbit interaction on the substrate atoms. We note in passing that CFEs can also lead to anisotropic SOC in Eq. (3) [47]. Such (usually small) anisotropy is neglected here since its main effect is simply a modulation of the magnitude of the effective SOCs on graphene.

We consider two types of commensurate substrates. In the first type, transition-metal atoms of a given species are placed at distance d above the center of a hexagonal plaquette in graphene (hollow position h in Fig. 2). In the second type, the atoms are located at a distance d above a carbon atom (top position). The unit cell of graphene is formed by two sublattices, and as such, there are two possible top configurations: t_A and t_B (see Fig. 3). The eigenstates of the first term [Eq. (2)] in space representation can be written as

$$\langle \vec{r}|d_l\rangle = R(r)\chi_l(\theta,\phi), \tag{4}$$

where $R(r)$ is the radial part of the wave function and $\chi_l(\theta,\phi) = \langle\theta,\phi|d_l\rangle$ ($l = z^2,xz,yz,xy,x^2 - y^2$) are tesseral harmonics. Unlike spherical harmonics (eigenfunctions of l_z), tesseral harmonics are real functions and do not have spherical symmetry.

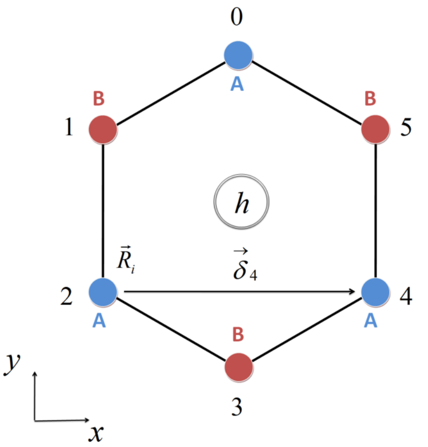

FIG. 2. Hollow position h. The j-index convention is used in Eqs. (11) and (A1)–(A5) and in the definitions of $\vec{\delta}_j$ and the direction cosines n_x^h,n_y^h, and n_z^h.

For calculation purposes, we recast the wave functions (we omit the radial part hereafter) in terms of eigenstates of l_z as

$$|d_{z^2}\rangle = |2,0\rangle, \tag{5}$$

$$|d_{xz}\rangle = \frac{1}{\sqrt{2}}(-|2,1\rangle + |2,-1\rangle), \tag{6}$$

$$|d_{yz}\rangle = \frac{\imath}{\sqrt{2}}(|2,1\rangle + |2,-1\rangle), \tag{7}$$

$$|d_{xy}\rangle = \frac{\imath}{\sqrt{2}}(-|2,2\rangle + |2,-2\rangle), \tag{8}$$

$$|d_{x^2-y^2}\rangle = \frac{1}{\sqrt{2}}(|2,2\rangle + |2,-2\rangle). \tag{9}$$

Below, we show that the main effect of the hybridization of graphene orbitals with nonspherically symmetric states of the substrate is to induce anisotropic SOC.

III. EFFECTIVE HAMILTONIAN: HOLLOW POSITION

As a simple model for the substrate, we consider a monolayer of heavy atoms sitting at the hollow sites. The d orbitals of each substrate atom hybridize with the p_z states of the nearest six carbon atoms (other hoppings are much smaller and thus are neglected). The hybridization Hamiltonian is $H_V^{\rm h} = T_{\rm h} + T_{\rm h}^\dagger$, with

$$T_{\rm h} = \sum_{\vec{R}_i}\sum_{l}\sum_{s=\uparrow,\downarrow} |\Phi_{s,l}(\vec{R}_i)\rangle\langle d_l,s,\vec{R}_i + \vec{h}|, \tag{10}$$

where $\vec{R}_i$ are lattice vectors, $\vec{h}$ is the position of h inside the plaquette, $s = \pm 1$ for up and down states, respectively, and

$$|\Phi_{s,l}(\vec{R}_i)\rangle = \sum_{j=0}^{5} t_{l,s,j}|\sigma_j,s,\vec{R}_i + \vec{\delta}_j\rangle. \tag{11}$$

Here, $j = 0,\dots,5$ runs counterclockwise and follows the convention in Fig. 2 and $\sigma_j = A$ (B) for even (odd) j. The substrate-graphene hopping amplitudes are defined by $t_{l,s,j} = \langle\sigma_j,s,\vec{R}_i + \vec{\delta}_j|\hat{V}|d_l,s,\vec{R}_i + \vec{h}\rangle$, where $\vec{\delta}_j$ are vectors connecting neighboring carbon atoms [48] (see Fig. 2).

The hopping amplitudes are evaluated by means of the Slater-Koster approach [42,43],

$$\langle p_z|V|d_{xy}\rangle = n_x n_y n_z(\sqrt{3}V_{pd\sigma} - 2V_{pd\pi}), \tag{12}$$

$$\langle p_z|V|d_{x^2-y^2}\rangle = \frac{\sqrt{3}}{2}n_z\big(n_x^2 - n_y^2\big)V_{pd\sigma} - n_z(n_x^2 - n_y^2)V_{pd\pi}, \tag{13}$$

$$\langle p_z|V|d_{zx}\rangle = \sqrt{3}n_z^2 n_x V_{pd\sigma} + \big(1 - 2n_z^2\big)n_x V_{pd\pi}, \tag{14}$$

$$\langle p_z|V|d_{zy}\rangle = \sqrt{3}n_z^2 n_y V_{pd\sigma} + \big(1 - 2n_z^2\big)n_y V_{pd\pi}, \tag{15}$$

$$\begin{aligned}\langle p_z|V|d_{z^2}\rangle &= \sqrt{3}n_z\big(n_x^2 + n_y^2\big)V_{pd\pi}\\ &\quad - \frac{1}{2}n_z\big(n_x^2 + n_y^2 - 2n_z^2\big)V_{pd\sigma},\end{aligned} \tag{16}$$

where $V_{pd\sigma}$ and $V_{pd\pi}$ are two-center integrals, which can be obtained by quantum chemistry methods or by fitting to first-principles electronic structure calculations [49,50]. n_i are direction cosines of the vector connecting a j-carbon atom and the substrate atom at the h position. The hopping amplitudes are given in the Appendix.

We are interested in the low-energy theory near the Dirac points $\vec{K} = -\vec{K}' = \frac{4\pi}{3a}\hat{x}$. The Fourier transform of the hopping matrix at these points can be easily computed, and we obtain, for each valley ($\tau = \pm 1$),

$$\begin{aligned}T_{\rm h} = \sum_{s=\uparrow,\downarrow} &\imath\tau\frac{3V_1}{\sqrt{2}}e^{\imath\tau 2\pi/3}(|A,s\rangle + |B,s\rangle)\langle d_{xz},s|\\ &+ \frac{3V_1}{\sqrt{2}}e^{\imath\tau 2\pi/3}(|A,s\rangle - |B,s\rangle)\langle d_{yz},s|\\ &+ \imath\tau\frac{3V_2}{\sqrt{2}}e^{\imath\tau 2\pi/3}(|B,s\rangle - |A,s\rangle)\langle d_{xy},s|\\ &- \frac{3V_2}{\sqrt{2}}e^{\imath\tau 2\pi/3}(|B,s\rangle + |A,s\rangle)\langle d_{x^2-y^2},s|.\end{aligned} \tag{17}$$

The various constants read $V_0 = \sqrt{3}n(1 - n^2)V_{pd\pi} - \frac{1}{2}n(1 - 3n^2)V_{pd\sigma}$, $V_1 = \frac{1}{\sqrt{2}}\sqrt{1 - n^2}(\sqrt{3}n^2 V_{pd\sigma} + (1 - 2n^2)V_{pd\pi})$, and $V_2 = \frac{1}{\sqrt{2}}n(1 - n^2)(\sqrt{3}V_{pd\sigma}/2 - V_{pd\pi})$, where $n_z^h = n = a_0/\sqrt{a_0^2 + d^2}$, with a_0 being the distance between two carbon atoms.

Next, we use degenerate perturbation theory to obtain a graphene-only effective Hamiltonian,

$$\begin{aligned}H_{\rm eff}^{\rm h} &= -T_{\rm h}(H_0 + H_{\rm so})^{-1}T_{\rm h}^\dagger\\ &\approx -T_{\rm h}H_0^{-1}T_{\rm h}^\dagger + T_{\rm h}H_0^{-1}H_{\rm so}H_0^{-1}T_{\rm h}^\dagger,\end{aligned} \tag{18}$$

where we treated the spin-orbit term of the substrate Hamiltonian $H_{\rm so}$ as a next-order perturbation compared to H_0. The first term $H_{\rm h}^{\rm CF} = -T_{\rm h}H_0^{-1}T_{\rm h}^\dagger$ can be expressed in terms of Pauli matrices:

$$H_{\rm h}^{\rm CF} = -\lambda_0 - \lambda_x\sigma_x, \tag{19}$$

with

$$\lambda_{0(x)} = \frac{9(V_1)^2}{2\epsilon_{xz}} \pm \frac{9(V_1)^2}{2\epsilon_{yz}} + \frac{9(V_2)^2}{2\epsilon_{xy}} \pm \frac{9(V_2)^2}{2\epsilon_{x^2-y^2}}. \tag{20}$$

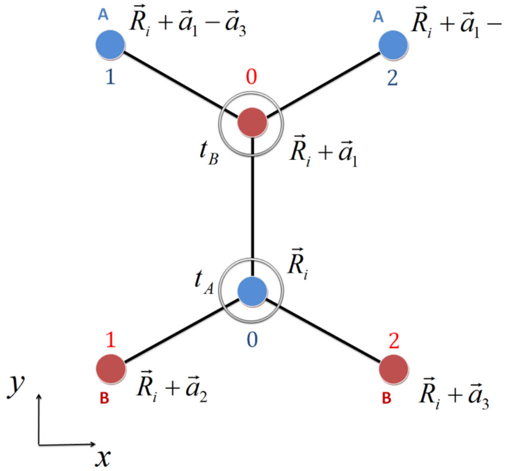

FIG. 3. Unit cell formed by atom A at position $\vec{R}_i$ and atom B at position $\vec{R}_i+\vec{a}_1$. Atom $t_{A(B)}$ hybridizes with graphene site $\vec{R}_i$ $(\vec{R}_i+\vec{a}_1)$ [on sublattice A (B)] and the three first neighboring sites on sublattice B (A). Red (blue) numbers on B (A) sites define the j-index convention used in states $|\Phi^{1A(B)}_{s,l}(\vec{R}_i)\rangle$ and hopping terms of Eqs. (A12)–(A16) [Eqs. (A17)–(A21)].

The first term in Eq. (19) is a trivial energy shift. The interaction λ_x is an orbital term, which can be absorbed by a redefinition of k_x in Eq. (1). The interplay between SOC and CFE is captured by the second term, $H_{\rm h}^{\rm CF/SO}=T_{\rm h}H_0^{-1}H_{so}H_0^{-1}T_{\rm h}^{\dagger}$, which has the form

$$\begin{aligned}H_{\rm h}^{\rm CF/SO}&=-\lambda^1_{\rm R}\sigma_y s_x-\lambda^2_{\rm R}\tau_z\sigma_x s_y\\&\quad+\lambda_{\rm KM}\tau_z\sigma_z s_z+\lambda^y_{\rm sv}\tau_z s_y,\end{aligned}\tag{21}$$

with couplings determined by

$$\lambda^1_{\rm R}=18\xi V_1V_2\left(\frac{1}{\epsilon_{xy}\epsilon_{xz}}+\frac{1}{\epsilon_{yz}\epsilon_{x^2-y^2}}\right),\tag{22}$$

$$\lambda^2_{\rm R}=18\xi V_1V_2\left(\frac{1}{\epsilon_{xy}\epsilon_{yz}}+\frac{1}{\epsilon_{xz}\epsilon_{x^2-y^2}}\right),\tag{23}$$

$$\lambda_{\rm KM}=9\xi\left(\frac{(V_1)^2}{\epsilon_{yz}\epsilon_{xz}}-\frac{2(V_2)^2}{\epsilon_{xy}\epsilon_{x^2-y^2}}\right),\tag{24}$$

$$\lambda^y_{\rm sv}=9\xi V_1V_2\left(\frac{1}{\epsilon_{xy}\epsilon_{yz}}-\frac{1}{\epsilon_{xz}\epsilon_{x^2-y^2}}\right).\tag{25}$$

The first two terms in Eq. (21) form an anisotropic Bychkov-Rashba coupling. The third term is the familiar intrinsiclike SOC. The last term is an in-plane spin-valley coupling, leading to an anisotropic spectrum. Note that this term vanishes in the absence of crystal-field splitting. Equations (19) and (21) are invariant under time-reversal symmetry ($\mathcal{T}: i\tau_x s_y K$) and the symmetry operations of the C_{2v} point group: twofold rotations around the z axis ($C_2: i\tau_x\sigma_x s_z$) and reflections over vertical planes xz ($\sigma_{\rm v}:\sigma_x s_y$) and yz ($\sigma'_{\rm v}:\tau_x s_x$) [40]. The point-group symmetry reduction to C_{2v} is a consequence of the hybridization of graphene's π states with nonspherically symmetric states in the substrate (5)–(9). The same effective couplings of Eqs. (19) and (21) were obtained in Ref. [40] for graphene on a Pb substrate in the absence of CFE due to the reduced point-group symmetry C_{2v} of the underlying superlattice.

IV. EFFECTIVE HAMILTONIAN: TOP POSITION

We assume that the top positions (t_A and t_B) are occupied by different atomic species (or, equivalently, equal species placed at different distances from graphene). This accounts for the important class of a graphene interface with reduced point-group symmetry C_{3v} (in the absence of CFE). Such a sublattice-dependent interaction was absent in the hollow-position case. The hybridization between p_z orbitals of graphene and d atoms on the top position can be written as $H_V=T_{\rm t}+T_{\rm t}^{\dagger}$, where the hopping matrix T_t is given by

$$\begin{aligned}T_{\rm t}=\sum_{\vec{R}_i}\sum_{l}\sum_{s=\uparrow,\downarrow}&\left[\left|\Phi^{(0,A)}_{s,l}(\vec{R}_i)\right\rangle+\left|\Phi^{(1,A)}_{s,l}(\vec{R}_i)\right\rangle\right]\langle d_l,s,A,\vec{R}_i|\\&+\left[\left|\Phi^{(0,B)}_{s,l}(\vec{R}_i)\right\rangle+\left|\Phi^{(1,B)}_{s,l}(\vec{R}_i)\right\rangle\right]\langle d_l,s,B,\vec{R}_i+\vec{a}_1|\end{aligned}\tag{26}$$

and the Φ states are defined in a way a similar to the hollow-position case, namely,

$$\left|\Phi^{(0,A)}_{s,l}(\vec{R}_i)\right\rangle=t^{(0,A)}_{l,s}\left|A,s,\vec{R}_i\right\rangle,\tag{27}$$

$$\left|\Phi^{(1,A)}_{s,l}(\vec{R}_i)\right\rangle=\sum_{j=0}^{2}t^{(1,A)}_{l,s,j}|B,s,\vec{R}_i+\vec{a}_{j+1}\rangle,\tag{28}$$

where $t^{(0,A)}_{l,s}=\langle A,s,\vec{R}_i|V|d_l,s,A,\vec{R}_i\rangle$ and $t^{(1,A)}_{l,s,j}=\langle B,s,\vec{R}_i+\vec{a}_{j+1}|V|d_l,s,A,\vec{R}_i\rangle$. Similar definitions are employed for states $|\Phi^{(0/1,A/B)}_{s,l}(\vec{R}_i)\rangle$ in Eq. (26).

The hopping parameters are written in the Appendix. Around K points in the hexagonal Brillouin zone, the hopping matrix can be written as $T_{\rm t}=\sum_{\tau=\pm1}T_{A{\rm t}}+T_{B{\rm t}}$, where

$$\begin{aligned}T_{\rm t}^{A(B)}=\sum_{s=\uparrow,\downarrow}&V_0^{0A(B)}|A(B),s\rangle\langle d_{z^2},s,A(B)|\\&\pm\frac{3V_1^{1A(B)}}{\sqrt{2}}|B(A),s\rangle\langle d_{yz},s,A(B)|\\&+\imath\tau\frac{3V_1^{1A(B)}}{\sqrt{2}}|B(A),s\rangle\langle d_{xz},s,A(B)|\\&-\frac{3V_2^{1A(B)}}{\sqrt{2}}|B(A),s\rangle\langle d_{x^2-y^2},s,A(B)|\\&\mp\imath\tau\frac{3V_2^{1A(B)}}{\sqrt{2}}|B(A),s\rangle\langle d_{xy},s,A(B)|,\end{aligned}\tag{29}$$

with the various constants given in the Appendix. Degenerate perturbation theory yields

$$\begin{aligned}H_{\rm t}^{\rm CF}&=-T_{\rm t}^{A}H_0^{-1}T_{\rm t}^{A\dagger}-T_{\rm t}^{B}H_0^{-1}T_{\rm t}^{B\dagger}\\&=-\tilde{\lambda}_0-\Delta\sigma_z,\end{aligned}\tag{30}$$

with coupling constants

$$\begin{aligned}\tilde{\lambda}_0=&\frac{\left(V_0^{0A}\right)^2}{2\epsilon^A_{z^2}}+\frac{9\left(V_1^{1A}\right)^2}{4\epsilon^A_{xz}}+\frac{9\left(V_1^{1A}\right)^2}{4\epsilon^A_{yz}}+\frac{9\left(V_2^{1A}\right)^2}{4\epsilon^A_{x^2-y^2}}\\&+\frac{9\left(V_2^{1A}\right)^2}{4\epsilon^A_{xy}}+(A\to B),\end{aligned}\tag{31}$$

$$\Delta = \frac{\left(V_0^{0A}\right)^2}{2\epsilon^A_{z^2}} - \frac{9\left(V_1^{1A}\right)^2}{4\epsilon^A_{xz}} - \frac{9\left(V_1^{1A}\right)^2}{4\epsilon^A_{yz}} - \frac{9\left(V_2^{1A}\right)^2}{4\epsilon^A_{x^2-y^2}} - \frac{9\left(V_2^{1A}\right)^2}{4\epsilon^A_{xy}} - (A \rightarrow B), \tag{32}$$

representing an energy shift and a staggered sublattice potential, respectively. The combined effect of crystal field and SOC can be written as

$$\begin{aligned} H_{\mathrm{t}}^{\mathrm{CF/SO}} &= T_{\mathrm{t}}^{A} H_0^{-1} H_{\mathrm{so}} H_0^{-1} T_{\mathrm{t}}^{A\dagger} + T_{\mathrm{t}}^{B} H_0^{-1} H_{\mathrm{so}} H_0^{-1} T_{\mathrm{t}}^{B\dagger} \\ &= -\tilde{\lambda}_{\mathrm{R}}^{1} \sigma_y s_x - \tilde{\lambda}_{\mathrm{R}}^{2} \tau_z \sigma_x s_y + \tilde{\lambda}_{\mathrm{KM}} \tau_z \sigma_z s_z \\ &\quad + \tilde{\lambda}_{\mathrm{sv}}^{z} \tau_z s_z + \tilde{\lambda}_{\mathrm{KM}}^{y} \tau_z \sigma_z s_y + \tilde{\lambda}_{\mathrm{sv}}^{y} \tau_z s_y, \end{aligned} \tag{33}$$

where the coupling constants are given by

$$\tilde{\lambda}_{\mathrm{R}}^{1} = 3\sqrt{6}\xi \left[\frac{V_0^{0A} V_1^{1A}}{\epsilon^A_{yz} \epsilon^A_{z^2}} + (A \rightarrow B) \right], \tag{34}$$

$$\tilde{\lambda}_{\mathrm{R}}^{2} = 3\sqrt{6}\xi \left[\frac{V_0^{0A} V_1^{1A}}{\epsilon^A_{xz} \epsilon^A_{z^2}} + (A \rightarrow B) \right], \tag{35}$$

$$\tilde{\lambda}_{\mathrm{KM}} = -9\xi \left[\frac{\left(V_1^{1A}\right)^2}{2\epsilon^A_{yz}\epsilon^A_{xz}} - \frac{\left(V_2^{1A}\right)^2}{\epsilon^A_{x^2-y^2}\epsilon^A_{xy}} + (A \rightarrow B) \right], \tag{36}$$

$$\tilde{\lambda}_{\mathrm{sv}}^{z} = 9\xi \left[\frac{\left(V_1^{1A}\right)^2}{2\epsilon^A_{yz}\epsilon^A_{xz}} - \frac{\left(V_2^{1A}\right)^2}{\epsilon^A_{x^2-y^2}\epsilon^A_{xy}} - (A \rightarrow B) \right], \tag{37}$$

$$\tilde{\lambda}_{\mathrm{KM}}^{y} = -\frac{9}{4}\xi \left[\frac{V_1^{1A} V_2^{1A}}{\epsilon^A_{xy}\epsilon^A_{yz}} - \frac{V_1^{1A} V_2^{1A}}{\epsilon^A_{x^2-y^2}\epsilon^A_{xz}} - (A \rightarrow B) \right], \tag{38}$$

$$\tilde{\lambda}_{\mathrm{sv}}^{y} = \frac{9}{4}\xi \left[\frac{V_1^{1A} V_2^{1A}}{\epsilon^A_{xy}\epsilon^A_{yz}} - \frac{V_1^{1A} V_2^{1A}}{\epsilon^A_{x^2-y^2}\epsilon^A_{xz}} + (A \rightarrow B) \right]. \tag{39}$$

In addition to the SOCs already obtained in the hollow case, the combination of a sublattice-dependent interaction and CFE gives rise to new terms. We obtain the expected spin-valley coupling $\tilde{\lambda}_{\mathrm{sv}}^{z} \tau_z s_z$, which together with the Bychkov-Rashba SOC is the dominant spin-orbit interaction in group-VI TMD-graphene bilayers [24,37]. Interestingly, the broken orbital degeneracy in the substrate also generates an in-plane intrinsic spin-orbit coupling $\tilde{\lambda}_{\mathrm{KM}}^{y} \tau_z \sigma_z s_y$. This term can open a quantum spin Hall insulating gap that is robust against Bychkov-Rashba SOC. A more detailed analysis of the effect of this interaction will be given in the next section.

It is instructive to consider two different limiting cases. First, we consider the situation where all the energies of d orbitals of the substrate are degenerate, i.e., the absence of a CFE. By analyzing the coupling constants in equations (34)–(39) the only couplings that remain are the familiar isotropic Bychkov-Rashba coupling, intrinsiclike SOC, and the spin-valley term. These same couplings were obtained for TMD-graphene heterostructures [24,37] and enable interesting spin-dependent phenomena, such as the anisotropic spin lifetime [27], spin Hall effect [31], and inverse spin-galvanic effect [32]. The second limit case is when top positions t_A and t_B are equivalent, so that one has $V_0^{0A} = V_0^{0B}$, $V_1^{1A} = V_1^{1B}$, and $V_2^{1A} = V_2^{1B}$. For this situation the SOCs that appear are the same as in Eq. (21) for the hollow-position case due to the restoration of sublattice symmetry.

Finally, we classify the SOCs in Eq. (33) according to the irreducible representations of graphene's full point group $C_{6v}^{''}$ (i.e., the direct product of C_{6v} and two primitive translation operations) and also the parity over mirror inversion symmetry ($z \rightarrow -z$). Following the notation of Ref. [51] (see also Ref. [52]), the in-plane intrinsic-type term ($\tilde{\lambda}_{\mathrm{KM}}^{y} \sigma_z \tau_z s_y$) transforms according to the E_1 irreducible representation (Irrep), and the in-plane spin-valley term ($\tilde{\lambda}_{\mathrm{sv}}^{y} \tau_z s_y$) transforms according to the E_2 Irrep of $C_{6v}^{''}$, and both are antisymmetric with respect to $z \rightarrow -z$ transformation. The familiar intrinsic-type SOC ($\tilde{\lambda}_{\mathrm{KM}} \tau_z \sigma_z s_z$) transforms according to the A_1 Irrep of $C_{6v}^{''}$, and the spin-valley SOC ($\tilde{\lambda}_{\mathrm{sv}} \tau_z s_z$) transforms according to the B_2 Irrep. Both are symmetric under the $z \rightarrow -z$ transformation. The anisotropic Rashba SOC can be decomposed into a term $\tau_z \sigma_x s_y - \sigma_y s_x$, which transforms according to the A_1 Irrep, and a term $\tau_z \sigma_x s_y + \sigma_y s_x$, which transforms according to the E_2 Irrep. Both are asymmetric under mirror inversion.

V. DISCUSSION

This paper aims to explore the modifications to the electronic states of graphene placed on a substrate characterized by a crystal-field environment. In a realistic scenario, we expect the proximity-induced SOC to be sensitive to the type of crystal-field splitting and the valence of the substrate atoms. A quantitative analysis is beyond the scope of this work. Nevertheless, the crystal field is expected to be significant in compounds containing transition-metals atoms, in which the incomplete outer shell is formed by d electrons. The electronic structure of certain TMDs is known to be strongly affected by CFE on the atomic states of transition-metal (TM) atoms [53,54]. TMD layers consist of a hcp sheet of TM atoms sandwiched between sheets of chalcogen atoms, and their metal coordination can be either trigonal prismatic or octahedral. In the trigonal prismatic coordination, the two chalcogen sheets are stacked directly above each other (known as the H phase). The stacking order in the octahedral phase (T phase) is ABC, and the chalcogen atoms of one of the sheets can be located at the center of the honeycomb lattice. In this case, the coordination of the TM atoms is octahedral.

Group-IV TMDs have an octahedral structure, whereas group-VI TMDs, of the well-studied W and Mo compounds, tend to display a trigonal prismatic geometry and both octahedral and trigonal prismatic phases are observed in group-V TMDs. The *trigonal prismatic geometry* enforces a splitting of d orbitals in a single state, d_{z^2}, and two doublets, $d_{x^2-y^2}/d_{xy}$ and d_{xz}/d_{yz}. On the other hand, in the *octahedral* geometry, a doublet, $d_{z^2}/d_{x^2-y^2}$, and a triplet, $d_{xy}/d_{xz}/d_{yz}$, are formed. Going back to Eqs. (21) and (33), one can see that the main signatures of the CFE is the broken rotational symmetry in the continuum due to the hybridization of graphene with states without spherical symmetry. The latter results in an in-plane spin-valley coupling $\lambda_{\mathrm{sv}}^{y} \tau_z s_y$ and an anisotropic Bychkov-Rashba SOC. For both top- and hollow-position cases, it is necessary that $\epsilon_{xy}\epsilon_{yz} \neq \epsilon_{x^2-y^2}\epsilon_{xz}$ for the appearance of the in-plane spin-valley coupling, which is the case for TM atoms with an *octahedral* distortion [see Fig. 1(a)]. This type of crystal field is found in the group-IV family (XY_2, where

X = Zr, Hf, and Y = S, Se, Te) and opens up the possibility to observe this coupling in bilayers of these materials and graphene. Less attention has been paid to this family [55,56] compared to group-V and -VI TMDs. The application of Zr-based chalcogenides in solar-energy devices has been suggested [56], and the possibility of tuning its properties by pressure, electric field, and phase engineering was recently explored in density functional theory calculations [57]. Our findings suggest that TMDs of family IV are potential candidates to induce nontrivial spin textures in graphene via proximity coupling. On the other hand, the anisotropic Bychkov-Rashba coupling requires $\epsilon_{xz} \neq \epsilon_{yz}$, which is only possible in a very low symmetry environment. The low-symmetry T′ phase in WTe$_2$ monolayers, which presents a quantum spin Hall phase [58,59], could induce an anisotropic Rashba coupling in graphene. This type of anisotropy can lead to an increase in the spin Hall angle in graphene decorated with SOC impurities [60].

For large interlayer distances, the overlap matrix between states centered on different atomic positions can be neglected, and we can use Eqs. (22)–(25) and (34)–(39) to perform a rough estimative of the different SOCs. Using Slater-Koster parameters for TM-carbon bonds as reported in Ref. [61] and the crystal-field splitting and spin-orbit energy ξ reported in Ref. [56], we estimate the graphene effective SOCs for distances ≈ 5 times graphene's lattice spacing. The dominant SOCs are found to be intrinsic-type and Rashba couplings, with an estimated magnitude in the range 20–40 meV for both hollow and top substrate atoms, which is consistent with the robust weak antilocalization features in magnetocondutance measurements [25]. The in-plane spin-valley SOC λ_{sv}^{y} is one order of magnitude weaker, being ≈2.5 meV for the hollow-position case and ≈1.2 meV for the top-position case (when atoms A and B have the same nature), which suggests a small but observable effect. For short graphene-substrate separations, numerical estimations need to take into account the overlap matrix between states at different atomic positions, which is beyond the scope of the present work. Note that the interlayer distance can be tuned by external pressure [57], which can be employed to tailor the SOC. Figure 4 shows the low-energy spectrum along the k_x direction when graphene has an effective SOC formed by Rashba, intrinsic-type, and in-plane spin-valley interactions. We see an interesting feature on this spectrum: the energy dispersion around inequivalent valleys is shifted (along the k_x direction) with respect to the bare graphene Dirac spectrum. This shift has opposite signs at inequivalent valleys as required by time-reversal symmetry.

Finally, we discuss the in-plane spin-orbit interaction $\lambda_{\text{KM}}^{y}\tau_z\sigma_z s_y$ in Eq. (33). In our estimate for group-IV TMD-graphene bilayers this type of coupling is relatively weak, being of the same order as the in-plane spin-valley term (≈1 meV). However, it has interesting topological properties. As mentioned above, this SOC can induce a nontrivial topological insulating gap associated with a $\mathbb{Z}_2$ topological invariant [62]. However, the robustness of the $\mathbb{Z}_2$ topological phase differs from that generated by the familiar intrinsic SOC in graphene λ_{KM} [33]. When only C_{6v}-invariant SOCs are present, that is, λ_{KM} and λ_{R}, the quantum spin Hall gap closes if $|\lambda_{\text{R}}| > |\lambda_{\text{KM}}|$ [33], destroying the topological phase [see Fig. 5(a)]. On the other hand, if the $\mathbb{Z}_2$ topological phase is a consequence of λ_{KM}^{y},

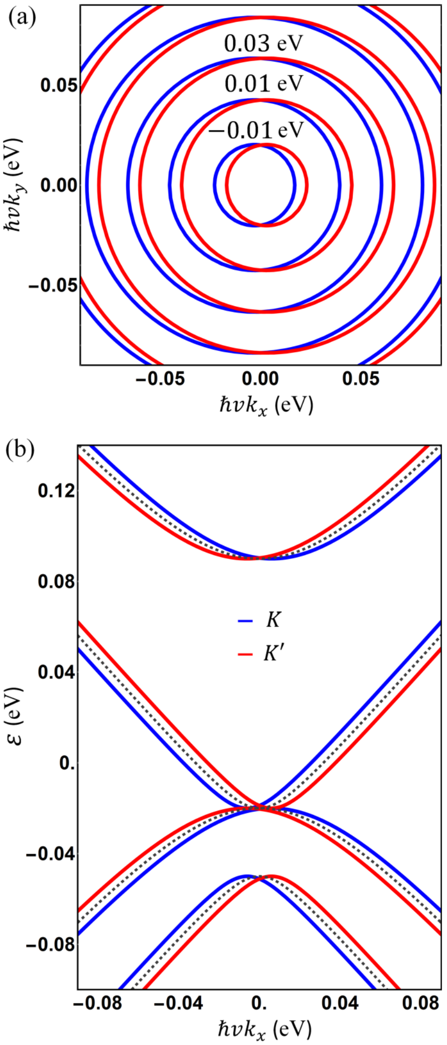

FIG. 4. (a) Fermi surface contours around K (K') points. (b) Low-energy spectrum along the k_x direction ($k_y = 0$). Parameters: $\lambda_{\text{sv}}^{y} = 6$ meV, $\lambda_{\text{R}}^{1} = \lambda_{\text{R}}^{2} = 35$ meV, and $\lambda_{\text{KM}} = 20$ meV.

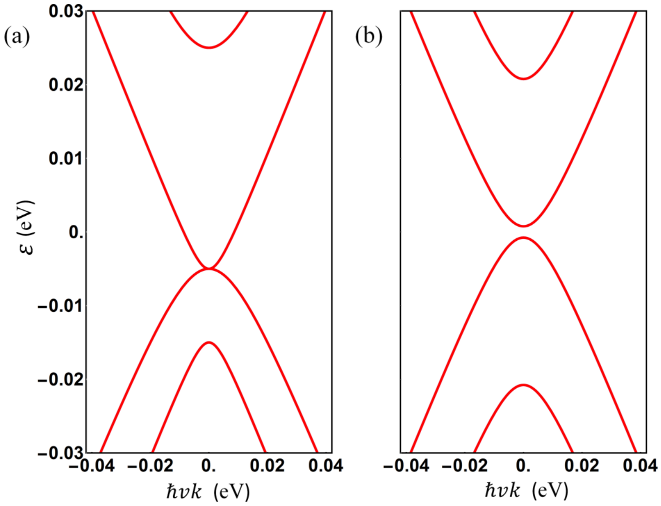

FIG. 5. Energy spectrum of graphene placed on a high-SOC substrate with a crystal-field environment. (a) $\lambda_{\text{R}} = 10$ meV, $\lambda_{\text{KM}} = 5$ meV and (b) $\lambda_{\text{R}} = 10$ meV, $\lambda_{\text{KM}}^{y} = 5$ meV. The gap has a nontrivial $\mathbb{Z}_2$ topological character corresponding to a quantum spin Hall phase.

the gap remains finite for *any* value of λ_{R} as long as $|\lambda_{\mathrm{sv}}^{y}| < |\lambda_{\mathrm{KM}}^{y}|$. A typical band structure is shown in Fig. 5(b), where the topological gap is finite even for large Bychkov-Rashba coupling. λ_{R} is one of the main obstacles to the observation of the quantum spin Hall effect in graphene because of its interplay with λ_{KM}. Our analysis suggests that realistic hybrid graphene-TMD bilayers can host a novel type of quantum spin Hall insulator with fully in plane helical edge states.

VI. CONCLUSION

We studied theoretically proximity spin-orbital effects in graphene placed on low-symmetry substrates with broken orbital degeneracy. We derived a low-energy (long-wavelength) theory for an idealized monolayer substrate, which allowed us to demonstrate a simple mechanism to remove the rotational invariance of electronic states in proximity-coupled graphene, i.e., their hybridization to crystal-field split states. The low-symmetry environment was shown to render spin-orbit interactions of π electrons highly anisotropic. The most distinctive signature of the crystal-field effect is the appearance of in-plane Zeeman spin-valley interaction $\lambda_{\mathrm{sv}}^{y}$ and anisotropic intrinsic-type spin-orbit coupling $\lambda_{\mathrm{KM}}^{y}$, which can drive a transition to a quantum spin Hall insulating phase displaying in-plane helical edge states. As a possible candidate to observe the predicted effects, we suggested group-IV TMD monolayers, where transition-metal atoms have an octahedral distortion and contain the necessary ingredients to induce anisotropic in-plane SOCs on graphene.

ACKNOWLEDGMENTS

T.G.R. acknowledges the support from the Newton Fund and the Royal Society (United Kingdom) through the Newton Advanced Fellowship scheme (reference NA150043); T.P.C. and T.G.R. thank the Brazilian Agency CNPq for financial support. A.F. gratefully acknowledges the support from the Royal Society (United Kingdom) through a Royal Society University Research Fellowship.

APPENDIX: HOPPING PARAMETERS AND Φ STATES

The explicit expressions for the hopping parameters in Eq. (11) for the hollow-position case are

$$t_{z^2,s,j} = V_0, \tag{A1}$$

$$t_{xz,s,j} = i\frac{V_1}{\sqrt{2}}(e^{i\pi j/3} - e^{-i\pi j/3}), \tag{A2}$$

$$t_{yz,s,j} = \frac{V_1}{\sqrt{2}}(e^{i\pi j/3} + e^{-i\pi j/3}), \tag{A3}$$

$$t_{xy,s,j} = i\frac{V_2}{\sqrt{2}}(e^{i2\pi j/3} - e^{-i2\pi j/3}), \tag{A4}$$

$$t_{x^2-y^2,s,j} = -\frac{V_2}{\sqrt{2}}(e^{i2\pi j/3} + e^{-i2\pi j/3}), \tag{A5}$$

with constants V_0, V_1, and V_2 given in Sec. III. The Φ states in Eq. (11) can be written in terms of hexagonal states,

$$\big|\Omega_m^s(\vec{R}_i)\big\rangle = \sum_{j=0}^{5} e^{im\pi j/3}|\sigma_j, s, \vec{R}_i + \vec{\delta}_j\rangle, \tag{A6}$$

with well-defined angular momentum $l_z = \hbar m$, and are described in Refs. [34,63]. Using Eqs. (A1)–(A5), we have

$$|\Phi_{z^2,s}(\vec{R}_i)\rangle = V_0\big|\Omega_0^s(\vec{R}_i)\big\rangle, \tag{A7}$$

$$|\Phi_{xz,s}(\vec{R}_i)\rangle = \imath\frac{V_1}{\sqrt{2}}\big[\big|\Omega_1^s(\vec{R}_i)\big\rangle - \big|\Omega_{-1}^s(\vec{R}_i)\big\rangle\big], \tag{A8}$$

$$|\Phi_{yz,s}(\vec{R}_i)\rangle = \frac{V_1}{\sqrt{2}}\big[\big|\Omega_1^s(\vec{R}_i)\big\rangle + \big|\Omega_{-1}^s(\vec{R}_i)\big\rangle\big], \tag{A9}$$

$$|\Phi_{xy,s}(\vec{R}_i)\rangle = \imath\frac{V_2}{\sqrt{2}}\big[\big|\Omega_2^s(\vec{R}_i)\big\rangle - \big|\Omega_{-2}^s(\vec{R}_i)\big\rangle\big], \tag{A10}$$

$$|\Phi_{x^2-y^2,s}(\vec{R}_i)\rangle = -\frac{V_2}{\sqrt{2}}\big[\big|\Omega_2^s(\vec{R}_i)\big\rangle + \big|\Omega_{-2}^s(\vec{R}_i)\big\rangle\big]. \tag{A11}$$

We now switch gears to the top-position case. Due to conservation of angular momentum, $t_{l,s}^{(0,A)}$ and $t_{l,s}^{(0,B)}$ are nonzero only for $l = z^2$, $t_{l,s}^{(0,A)} = V_0^{0A} = V_{pd\sigma}^{0A}$, and $t_{l,s}^{(0,B)} = V_0^{0B} = V_{pd\sigma}^{0B}$. The explicit expressions of $t_{l,s,j}^{(1,A)}$ are

$$t_{z^2,s,j}^{(1A)} = V_0^{1A}, \tag{A12}$$

$$t_{xz,s,j}^{(1A)} = V_1^{1A}\frac{\imath}{\sqrt{2}}(e^{2\pi\imath j/3} - e^{-2\pi\imath j/3}), \tag{A13}$$

$$t_{yz,s,j}^{(1A)} = V_1^{1A}\frac{1}{\sqrt{2}}(e^{2\pi\imath j/3} + e^{-2\pi\imath j/3}), \tag{A14}$$

$$t_{xy,s,j}^{(1A)} = -V_2^{1A}\frac{\imath}{\sqrt{2}}(-e^{4\pi\imath j/3} + e^{-4\pi\imath j/3}), \tag{A15}$$

$$t_{x^2-y^2,s,j}^{(1A)} = -V_2^{1A}\frac{1}{\sqrt{2}}(e^{4\pi\imath j/3} + e^{-4\pi\imath j/3}). \tag{A16}$$

The explicit expressions of $t_{l,s,j}^{(1,B)}$ are

$$t_{z^2,s,j}^{(1B)} = V_0^{1B}, \tag{A17}$$

$$t_{xz,s,j}^{(1B)} = V_1^{1B}\frac{\imath}{\sqrt{2}}(-e^{-2\pi\imath j/3} + e^{2\pi\imath j/3}), \tag{A18}$$

$$t_{yz,s,j}^{(1B)} = -V_1^{1B}\frac{1}{\sqrt{2}}(e^{-2\pi\imath j/3} + e^{2\pi\imath j/3}), \tag{A19}$$

$$t_{xy,s,j}^{(1B)} = -V_2^{1B}\frac{\imath}{\sqrt{2}}(-e^{-4\pi\imath j/3} + e^{4\pi\imath j/3}), \tag{A20}$$

$$t_{x2-y^2,s,j}^{(1B)} = -V_2^{1B}\frac{1}{\sqrt{2}}(e^{-4\pi\imath j/3} + e^{4\pi\imath j/3}). \tag{A21}$$

The constants in Eqs. (A12)–(A16) are $V_0^{1A} = \sqrt{3}n_{1A}(1 - n_{1A}^2)V_{pd\pi}^{(1A)} - \frac{1}{2}n_{1A}(1 - 3n_{1A}^2)V_{pd\sigma}^{(1A)}$, $V_1^{1A} = \frac{1}{\sqrt{2}}[\sqrt{3}n_{1A}^2V_{pd\sigma}^{(1A)} + (1 - 2n_{1A}^2)V_{pd\pi}^{(1A)}]\sqrt{1 - n_{1A}^2}$, and $V_2^{1A} = \frac{1}{\sqrt{2}}n_{1A}(1 - n_{1A}^2)(\frac{\sqrt{3}}{2}V_{pd\sigma}^{(1A)} - V_{pd\pi}^{(1A)})$, and except for changing A to B, the constants are the same in (A17)–(A21).

The Φ states in Eq. (26) can be write in terms of triangular states [34],

$$\left|\Gamma_m^{s(1A)}(\vec{R}_i)\right\rangle = \sum_{j=0}^{2} e^{im2\pi j/3}|B,s,\vec{R}_i+\vec{a}_{j+1}\rangle, \tag{A22}$$

$$\left|\Gamma_m^{s(1B)}(\vec{R}_i)\right\rangle = \sum_{j=0}^{2} e^{im2\pi j/3}|A,s,\vec{R}_i+\vec{a}_1+\vec{\delta}_{j+1}\rangle. \tag{A23}$$

Here, $\vec{\delta}_j$ are given by $\vec{\delta}_1=-\vec{a}_1$, $\vec{\delta}_2=-\vec{a}_3$, and $\vec{\delta}_3=-\vec{a}_2$. States (A22) and (A23), similar to states (A6), have well-defined angular momentum and satisfy $|\Gamma_2\rangle=|\Gamma_{-1}\rangle$ and $|\Gamma_{-2}\rangle=|\Gamma_1\rangle$. In other words, graphene does not support triangular states with $|m|=2$ [34]. Finally, we find

$$\left|\Phi_{s,z^2}^{(1A)}(\vec{R}_i)\right\rangle = V_0^{1A}\left|\Gamma_0^{s(1A)}(\vec{R}_i)\right\rangle, \tag{A24}$$

$$\left|\Phi_{s,xz}^{(1A)}(\vec{R}_i)\right\rangle = V_1^{1A}\frac{\imath}{\sqrt{2}}\left[\left|\Gamma_1^{s(1A)}(\vec{R}_i)\right\rangle - \left|\Gamma_{-1}^{s(1A)}(\vec{R}_i)\right\rangle\right], \tag{A25}$$

$$\left|\Phi_{s,yz}^{(1A)}(\vec{R}_i)\right\rangle = V_1^{1A}\frac{1}{\sqrt{2}}\left[\left|\Gamma_1^{s(1A)}(\vec{R}_i)\right\rangle + \left|\Gamma_{-1}^{s(1A)}(\vec{R}_i)\right\rangle\right], \tag{A26}$$

$$\left|\Phi_{s,xy}^{(1A)}(\vec{R}_i)\right\rangle = -V_2^{1A}\frac{\imath}{\sqrt{2}}\left[-\left|\Gamma_{-1}^{s(1A)}(\vec{R}_i)\right\rangle + \left|\Gamma_1^{s(1A)}(\vec{R}_i)\right\rangle\right], \tag{A27}$$

$$\left|\Phi_{s,x^2-y^2}^{(1A)}(\vec{R}_i)\right\rangle = -V_2^{1A}\frac{1}{\sqrt{2}}\left[\left|\Gamma_{-1}^{s(1A)}(\vec{R}_i)\right\rangle + \left|\Gamma_1^{s(1A)}(\vec{R}_i)\right\rangle\right] \tag{A28}$$

and

$$\left|\Phi_{s,z^2}^{(1B)}(\vec{R}_i)\right\rangle = V_0^{1B}\left|\Gamma_0^{s(1B)}(\vec{R}_i)\right\rangle, \tag{A29}$$

$$\left|\Phi_{s,xz}^{(1B)}(\vec{R}_i)\right\rangle = V_1^{1B}\frac{\imath}{\sqrt{2}}\left[-\left|\Gamma_{-1}^{s(1B)}(\vec{R}_i)\right\rangle + \left|\Gamma_1^{s(1B)}(\vec{R}_i)\right\rangle\right], \tag{A30}$$

$$\left|\Phi_{s,yz}^{(1B)}(\vec{R}_i)\right\rangle = -V_1^{1B}\frac{1}{\sqrt{2}}\left[\left|\Gamma_{-1}^{s(1B)}(\vec{R}_i)\right\rangle + \left|\Gamma_1^{s(1B)}(\vec{R}_i)\right\rangle\right], \tag{A31}$$

$$\left|\Phi_{s,xy}^{(1B)}(\vec{R}_i)\right\rangle = -V_2^{1B}\frac{\imath}{\sqrt{2}}\left[-\left|\Gamma_1^{s(1B)}(\vec{R}_i)\right\rangle + \left|\Gamma_{-1}^{s(1B)}(\vec{R}_i)\right\rangle\right], \tag{A32}$$

$$\left|\Phi_{s,x^2-y^2}^{(1B)}(\vec{R}_i)\right\rangle = -V_2^{1B}\frac{1}{\sqrt{2}}\left[\left|\Gamma_1^{s(1B)}(\vec{R}_i)\right\rangle + \left|\Gamma_{-1}^{s(1B)}(\vec{R}_i)\right\rangle\right]. \tag{A33}$$

[1] P. Fazekas, *Lecture Notes on Electron Correlation and Magnetism* (World Scientific, Singapore, 1999).

[2] E. Dagotto, Rev. Mod. Phys. **66**, 763 (1994).

[3] F. C. Zhang and T. M. Rice, Phys. Rev. B **37**, 3759(R) (1988).

[4] R. Sachidanandam, T. Yildirim, A. B. Harris, A. Aharony, and O. Entin-Wohlman, Phys. Rev. B **56**, 260 (1997).

[5] P. Sati, R. Hayn, R. Kuzian, S. Regnier, S. Schafer, A. Stepanov, C. Morhain, C. Deparis, M. Laugt, M. Goiran, and Z. Golacki, Phys. Rev. Lett. **96**, 017203 (2006).

[6] S. Ishihara, J. Inoue, and S. Maekawa, Phys. Rev. B **55**, 8280 (1997).

[7] M. B. Salamon and M. Jaime, Rev. Mod. Phys. **73**, 583 (2001).

[8] H. A. Jahn and E. Teller, Proc. Roy. Soc. A **161**, 220 (1937).

[9] M. Ishizuka, I. Yamada, K. Amaya, and S. Endo, J. Phys. Soc. Jpn. **65**, 1927 (1996).

[10] G. A. Gehring and K. A. Gehring, Rep. Prog. Phys. **38**, 1 (1975).

[11] A. B. Cahaya, A. O. Leon, and G. E. W. Bauer, Phys. Rev. B **96**, 144434 (2017).

[12] D. Santos-Cottin, M. Casula, G. Lantz, Y. Klein, L. Petaccia, P. Le Fèvre, F. Bertran, E. Papalazarou, M. Marsi, and A. Gauzzi, Nat. Commun. **7**, 11258 (2016).

[13] C.-L. Song, Y.-L. Wang, Y.-P. Jiang, Y. Zhang, C.-Z. Chang, L. Wang, K. He, X. Chen, J.-F. Jia, Y. Wang, Z. Fang, X. Dai, X.-C. Xie, X.-L. Qi, S.-C. Zhang, Q.-K. Xue, and X. Ma, Appl. Phys. Lett. **97**, 143118 (2010).

[14] P. Lee, K.-H. Jin, S. J. Sung, J. G. Kim, M.-T. Ryu, H.-M. Park, S.-H. Jhi, N. Kim, Y. Kim, S. U. Yu, K. S. Kim, D. Y. Noh, and J. Chung, ACS Nano **9**, 10861 (2015).

[15] S. Rajput, Y.-Y. Li, M. Weinert, and L. Li, ACS Nano **10**, 8450 (2016).

[16] D. Xiao, G.-B. Liu, W. Feng, X. Xu, and W. Yao, Phys. Rev. Lett. **108**, 196802 (2012).

[17] Q. H. Wang, K. Kalantar-Zadeh, A. Kis, J. N. Coleman, and M. S. Strano, Nat. Nanotechnol. **7**, 699 (2012).

[18] K. F. Mak and J. Shan, Nat. Photonics **10**, 216 (2016).

[19] R. A. Muniz and J. E. Sipe, Phys. Rev. B **91**, 085404 (2015).

[20] M. Gmitra and J. Fabian, Phys. Rev. B **92**, 155403 (2015).

[21] A. Avsar, D. Unuchek, J. Liu, O. L. Sanchez, K. Watanabe, T. Taniguchi, B. Ozyilmaz, and A. Kis, ACS Nano **11**, 11678 (2017).

[22] Y. K. Luo, J. Xu, T. Zhu, G. Wu, E. J. McCormick, W. Zhan, M. R. Neupane, and R. K. Kawakami, Nano Lett. **17**, 3877 (2017).

[23] A. Avsar, J. Y. Tan, T. Taychatanapat, J. Balakrishnan, G. K. W. Koon, Y. Yeo, J. Lahiri, A. Carvalho, A. S. Rodin, E. C. T. O'Farrell, G. Eda, A. H. Castro Neto, and B. Ozyilmaz, Nat. Commun. **5**, 4875 (2014).

[24] Z. Wang, D.-K. Ki, H. Chen, H. Berger, A. H. MacDonald, and A. F. Morpurgo, Nat. Commun. **6**, 8339 (2015).

[25] Z. Wang, D.-K. Ki, J. Y. Khoo, D. Mauro, H. Berger, L. S. Levitov, and A. F. Morpurgo, Phys. Rev. X **6**, 041020 (2016).

[26] S. Zihlmann, A. W. Cummings, J. H. Garcia, M. Kedves, K. Watanabe, T. Taniguchi, C. Schönenberger, and P. Makk, Phys. Rev. B **97**, 075434 (2018).

[27] A. W. Cummings, J. H. Garcia, J. Fabian, and S. Roche, Phys. Rev. Lett. **119**, 206601 (2017).

[28] T. S. Ghiasi, J. Ingla-Aynes, A. Kaverzin, and B. J. van Wees, Nano Lett. **17**, 7528 (2017).

[29] L. A. Benítez, J. F. Sierra, W. S. Torres, A. Arrighi, F. Bonell, M. V. Costache, and S. O. Valenzuela, Nat. Phys. **14**, 303 (2018).

[30] S. Omar and B. J. van Wees, Phys. Rev. B **97**, 045414 (2018).

[31] M. Milletari, M. Offidani, A. Ferreira, and R. Raimondi, Phys. Rev. Lett. **119**, 246801 (2017).
[32] M. Offidani, M. Milletari, R. Raimondi, and A. Ferreira, Phys. Rev. Lett. **119**, 196801 (2017).
[33] C. L. Kane and E. J. Mele, Phys. Rev. Lett. **95**, 226801 (2005).
[34] A. Pachoud, A. Ferreira, B. Ozyilmaz, and A. H. Castro Neto, Phys. Rev. B **90**, 035444 (2014).
[35] D. Kochan, S. Irmer, and J. Fabian, Phys. Rev. B **95**, 165415 (2017).
[36] E. I. Rashba, Phys. Rev. B **79**, 161409(R) (2009).
[37] M. Gmitra, D. Kochan, P. Hogl, and J. Fabian, Phys. Rev. B **93**, 155104 (2016).
[38] B. Hunt, J. D. Sanchez-Yamagishi, A. F. Young, M. Yankowitz, B. J. LeRoy, K. Watanabe, T. Taniguchi, P. Moon, M. Koshino, P. Jarillo-Herrero, and R. C. Ashoori, Science **340**, 1427 (2013).
[39] J. Jung, A. M. DaSilva, A. H. MacDonald, and S. Adam, Nat. Commun. **6**, 6308 (2015).
[40] F. Calleja, H. Ochoa, M. Garnica, S. Barja, J. J. Navarro, A. Black, M. M. Otrokov, E. V. Chulkov, A. Arnau, A. L. V. de Parga, F. Guinea, and R. Miranda, Nat. Phys. **11**, 43 (2015).
[41] V. T. Phong, N. R. Walet, and F. Guinea, 2D Mater. **5**, 014004 (2017).
[42] J. C. Slater and G. F. Koster, Phys. Rev. **94**, 1498 (1954).
[43] W. A. Harrison, *Elementary Electronic Structure* (World Scientific, Singapore, 2004).
[44] G. Giovannetti, P. A. Khomyakov, G. Brocks, P. J. Kelly, and J. van den Brink, Phys. Rev. B **76**, 073103 (2007).
[45] The relative strength of the proximity interactions at low energy is determined by the details of the hybridization V between electronic states defined near the Dirac points ($\mathbf{k} = 0$), which is independent of the electronic dispersion away from those points.
[46] For convenience, the energy levels ϵ_{d_l} are defined with respect to the on-site energy of carbon atoms.
[47] F. J. dos Santos, D. A. Bahamon, R. B. Muniz, K. McKenna, E. V. Castro, J. Lischner, and A. Ferreira, arXiv:1712.07827.
[48] A. H. Castro Neto, F. Guinea, N. M. R. Peres, K. S. Novoselov, and A. K. Geim, Rev. Mod. Phys. **81**, 109 (2009).
[49] E. Cappelluti, R. Roldan, J. A. Silva-Guillen, P. Ordejon, and F. Guinea, Phys. Rev. B **88**, 075409 (2013).
[50] J. A. Silva-Guillen, P. San-Jose, and R. Roldan, Appl. Sci. **6**, 284 (2016).
[51] H. Ochoa, A. H. Castro Neto, V. I. Fal'ko, and F. Guinea, Phys. Rev. B **86**, 245411 (2012).
[52] J.-S. You, D.-W. Wang, and M. A. Cazalilla, Phys. Rev. B **92**, 035421 (2015).
[53] C. Gong, H. Zhang, W. Wang, L. Colombo, R. M. Wallace, and K. Cho, Appl. Phys. Lett **103**, 053513 (2013).
[54] Y. J. Zhang, M. Yoshida, R. Suzuki, and Y. Iwasa, 2D Mater. **2**, 044004 (2015).
[55] Y. Li, J. Kang, and J. Li, RSC Adv. **4**, 7396 (2014).
[56] H. Jiang, J. Chem. Phys. **134**, 204705 (2011).
[57] A. Kumar, H. He, R. Pandey, P. K. Ahluwalia, and K. Tankeshwar, Phys. Chem. Chem. Phys. **17**, 19215 (2015).
[58] X. Qian, J. Liu, L. Fu, and J. Li, Science **346**, 1344 (2014).
[59] S. Wu, V. Fatemi, Q. D. Gibson, K. Watanabe, T. Taniguchi, R. J. Cava, and P. Jarillo-Herrero, Science **359**, 76 (2018).
[60] H.-Y. Yang, C. Huang, H. Ochoa, and M. A. Cazalilla, Phys. Rev. B **93**, 085418 (2016).
[61] D. H. Le, C. Colinet, and A. Pasturel, Phys. B (Amsterdam, Neth.) **168**, 285 (1991).
[62] D. N. Sheng, Z. Y. Weng, L. Sheng, and F. D. M. Haldane, Phys. Rev. Lett. **97**, 036808 (2006).
[63] C. Weeks, J. Hu, J. Alicea, M. Franz, and R. Wu, Phys. Rev. X **1**, 021001 (2011).